PAPER

Inelastic resonant scattering of electrons on hydrogen-like ions

Physica Scripta

PAPER

Inelastic resonant scattering of electrons on hydrogen-like ions

D M Vasileva[1,2,*], K N Lyashchenko[1,2], O Yu Andreev[1,2] and D Yu[3,4]

[1] Department of Physics, St. Petersburg State University, 7/9 Universitetskaya nab., St. Petersburg, 199034, Russia
[2] Petersburg Nuclear Physics Institute named by B.P. Konstantinov of NationalResearch Centre Kurchatov Institute, Gatchina, Leningrad District 188300, Russia
[3] Institute of Modern Physics, Chinese Academy of Sciences, Lanzhou 730000, People's Republic of China
[4] University of Chinese Academy of Sciences, Beijing 100049, People's Republic of China
[*] Author to whom any correspondence should be addressed.

E-mail: summerdacha64@gmail.com

RECEIVED
4 July 2024

REVISED
26 September 2024

ACCEPTED FOR PUBLICATION
16 October 2024

PUBLISHED
30 October 2024

Keywords: electron scattering, highly charged ions, inelastic scattering, impact excitation, autoionizing states, first-principles calculation, relativistic and quantum electrodynamics effects

Supplementary material for this article is available online

Abstract

The inelastic electron scattering is one of the processes that must be understood in detail for the correct interpretation of astrophysical data. We suggest ab initio QED treatment of the inelastic scattering of quasi-free electrons on hydrogen-like ions with possible formation and subsequent decay of intermediate autoionizing states. We calculate the doubly differential cross sections for scattering on F^{8+}, Ca^{19+} and Kr^{35+} in the range of energies where doubly excited $3l3l'$ states are involved. The energies and widths of these states are presented.

1. Introduction

Highly charged ions with a small number of electrons occupy a significant place in atomic physics. In such ions, electrons move in a very strong electric field of the atomic nucleus, which for heavy ions is much stronger than the fields available in laboratory. The processes occurring in collisions of electrons and atoms with the highly charged ions are especially interesting as they allow us to verify the theoretical description of electrons in strong fields, in particular their correlation and dynamics.

The highly charged ions are widely used for the production of materials with a specific nanostructure [1, 2], obtaining sources of strong x-ray radiation [3] and in many other fields, including medicine. The study of highly charged ions is also necessary to describe the laboratory and astrophysical plasmas. The x-rays originating from the radiative decay of the excited states of highly charged ions are detected in the observations of astrophysical objects (for example, galaxy clusters). The resulting spectra provide important information about various characteristics of these objects such as temperature structure, density or metal abundances [4].

Electron impact excitation (or inelastic electron scattering) is an important mechanism of production of ions in excited states in astrophysical plasmas. In this process, an incident electron is scattered on an ion with one or more bound electrons transferring a portion of its energy to the ion causing its transition to an excited state. In the energy region considered in this work, three different channels occur with ion excitation from $1s$ to $2s$, $2p_{1/2}$ and $2p_{3/2}$.

The lines in x-ray spectra originating from hydrogen-like and helium-like ions are among the most prominent. The scattering of electrons by hydrogen-like and helium-like ions may lead to the formation of intermediate two-electron states, which are simple enough for an accurate theoretical description within the framework of QED. Nevertheless, the existing calculations employ the R-matrix method or the relativistic distorted wave approximation [5–10]. In these works, the total probability of ion excitation in plasmas of certain temperature was investigated. However, these approaches can give different values for collision strengths [4], especially for high temperature plasmas (i.e., for the collision energies where the relativistic effects are significant) and high Z ions. Accordingly, it would be beneficial to have a calculation method suitable for scattering on medium to high Z ions and for relativistic impact energies that has predictable accuracy.

The theoretical calculations as well as the experimental data for the doubly differential cross sections of the resonant inelastic electron scattering have so far been limited to light ions with Z up to 9 [11–15]. In these works, again the R-matrix approach is used for the theoretical description.

Recent developments in experimental apparatus at GSI in Germany [16] and at HIRFL and HIAF in China [17], which, in particular, resulted in the new opportunities for conducting scattering experiments with medium and high Z ions, have sparked a renewed interest in such experiments.

We present an *ab initio* QED treatment for the resonant inelastic scattering of quasi-free electrons on hydrogen-like ions that directly takes into account relativistic and QED effects and can therefore be applied to the inelastic electron scattering on ions with medium and large Z where these effects become important. We demonstrate the application of this approach to the description of the inelastic electron scattering by F^{8+}, Ca^{19+} and Kr^{35+} ions for the energy range where the intermediate autoionizing states can contribute to the process. For the low-Z ions, we compare our results with the available experimental and theoretical data showing that our method can also be successfully applied to the light systems.

The relativistic units are used throughout the paper.

2. Theory

In this work, we look into the inelastic scattering of electrons on hydrogen-like ions initially being in the ground state. We consider the excitation of the ion into the $2s$, $2p_{1/2}$ and $2p_{3/2}$ states. The inelastic electron scattering can be divided into two channels: the non-resonant channel

$$e^-_{\boldsymbol{p}_i} + X^{(Z-1)+}(1s) \longrightarrow e^-_{\boldsymbol{p}_f} + X^{(Z-1)+}(2l), \tag{1}$$

and the resonant channel, in which the scattering proceeds through formation and subsequent decay of intermediate autoionizing states

$$e^-_{\boldsymbol{p}_i} + X^{(Z-1)+}(1s) \longrightarrow X^{(Z-2)+}(3l3l') \longrightarrow e^-_{\boldsymbol{p}_f} + X^{(Z-1)+}(2l). \tag{2}$$

Here $\boldsymbol{p}_i$ and $\boldsymbol{p}_f$ are the incident and scattered electron momenta, respectively. We note that the Coulomb scattering of electron (the Mott scattering) does not change the energy of electron. Accordingly, this channel does not contribute to the inelastic scattering.

We focus our attention on the resonances corresponding to the excitation of $3l3l'$ doubly excited (autoionizing) states. In accordance with the energy conservation law the energies of the incident (ε_i) and scattered (ε_f) electron must satisfy the following equality

$$\varepsilon_i + \varepsilon_{1s} = \varepsilon_f + \varepsilon_{2l}, \tag{3}$$

where ε_{1s} is the initial energy of the ion ($1s$) and ε_{2l} is the final energy of the ion ($2s$, $2p_{1/2}$ or $2p_{3/2}$).

We introduce wave functions $\Psi^i_{m_i,\mu_i}$ and $\Psi^f_{m_f,\mu_f}$ describing the initial and final states of the two-electron system in the zeroth order of the perturbation theory:

$$\Psi^i_{m_i,\mu_i}(\boldsymbol{r}_1, \boldsymbol{r}_2) = \frac{1}{\sqrt{2}} \det\{\overset{(+)}{\underset{\boldsymbol{p}_i\mu_i}{\psi}}(\boldsymbol{r}_1), \psi_{1s}(\boldsymbol{r}_2)\}, \tag{4}$$

$$\Psi^f_{m_f,\mu_f}(\boldsymbol{r}_1, \boldsymbol{r}_2) = \frac{1}{\sqrt{2}} \det\{\overset{(-)}{\underset{\boldsymbol{p}_f\mu_f}{\psi}}(\boldsymbol{r}_1), \psi_{2l}(\boldsymbol{r}_2)\}, \tag{5}$$

where $\psi_{1s}(\boldsymbol{r})$ and $\psi_{2l}(\boldsymbol{r})$ are the wave functions of the bound states ($1s$ and $2s$, $2p_{1/2}$ or $2p_{3/2}$) in the hydrogen-like ion with the total angular momentum projections on z-axis m_i and m_f; $\psi^{(\pm)}_{\boldsymbol{p}\mu}(\boldsymbol{r})$ is the in- (+) or out-going (−) wave function of an electron in the electric field of the atomic nucleus with the asymptotic momentum ($\boldsymbol{p} = p\hat{\boldsymbol{\nu}}$) [18]:

$$\psi^{(\pm)}_{\boldsymbol{p}\mu_\zeta}(\boldsymbol{r}) = \frac{(2\pi)^{3/2}}{\sqrt{p\varepsilon}} \sum_{jlm} \Omega^+_{jlm}(\boldsymbol{\nu}) \nu_{\mu_\zeta} e^{\pm i\phi_{jl}} i^l \psi_{\varepsilon jlm}(\boldsymbol{r}), \tag{6}$$

where $\psi_{\varepsilon jlm}(\boldsymbol{r})$ is the continuum solution of the Dirac equation with certain parity, total angular momentum and its projection, ϕ_{jl} is the Coulomb phase shift [18]. The spinor ν_{μ_ζ} for a given direction $\hat{\boldsymbol{\zeta}}$ is determined by the following equation:

$$\frac{1}{2}(\hat{\boldsymbol{\zeta}}\boldsymbol{\sigma})\nu_{\mu_\zeta} = \mu_\zeta \nu_{\mu_\zeta}, \tag{7}$$

where $\boldsymbol{\sigma}$ is the Pauli vector.

For the description of the resonant channel we employ the line-profile approach (LPA) [19] which is suitable for the treatment of the quasi-degenerate states within the framework of QED. The application of the LPA to the

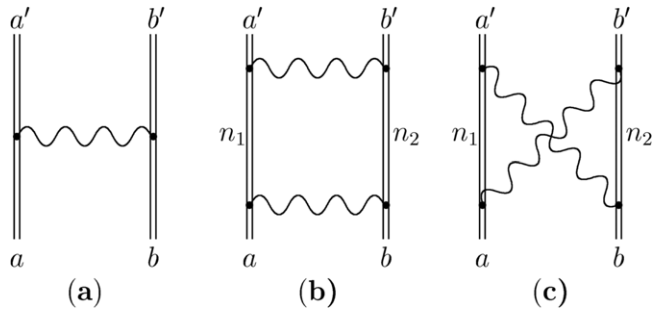

Figure 1. Feynman graphs corresponding to the one-photon (a) and two-photon (b and c) exchange corrections. The double solid lines denote the electrons in the external potential (the Furry picture); the internal wavy lines describe the exchange of the photon between two electrons; the indices n_1 and n_2 correspond to the intermediate one-electron states.

elastic electron scattering is discussed in detail in [20]. Within the LPA the matrix $V = V^{(0)} + \Delta V$ is introduced. The matrix $V^{(0)}$ is a diagonal matrix defined by

$$\hat{V}^{(0)} = \hat{h}_{\rm D}(\boldsymbol{r}_1) + \hat{h}_{\rm D}(\boldsymbol{r}_2). \tag{8}$$

Here $\hat{h}_{\rm D}$ is the Dirac Hamiltonian:

$$\hat{h}_{\rm D}(\boldsymbol{r}_i) = \boldsymbol{\alpha}\boldsymbol{p}_i + \beta m_e + V(\boldsymbol{r}_i), \quad i = 1, 2, \tag{9}$$

where $\boldsymbol{\alpha}$ and β are the Dirac matrices, m_e is the electron mass and $V(\boldsymbol{r}_i)$ is the potential energy of the electron in the electric field of the atomic nucleus. We take into account the interaction with the atomic nucleus in all orders by employing the Furry picture [21].

The matrix ΔV contains various QED corrections including the one- and two-photon exchange corrections, the electron self-energy and vacuum polarization corrections which are derived order by order within the QED perturbation theory. The Feynman graphs representing the one- and two-photon exchange corrections are presented in figure 1. It is convenient to present the matrix V as a block matrix

$$V = \begin{pmatrix} V_{11} & V_{12} \\ V_{21} & V_{22} \end{pmatrix} = \begin{pmatrix} V_{11}^{(0)} + \Delta V_{11} & \Delta V_{12} \\ \Delta V_{21} & V_{22}^{(0)} + \Delta V_{22} \end{pmatrix}, \tag{10}$$

where matrix V_{11} is a finite matrix defined on the given set G. The set G includes all two-electron configurations with energies close to the energies of the reference (initial and final) states. In particular, it contains all two-electron configurations consisting of electrons with principal quantum numbers $n \leqslant N_g$ (calculations were performed for $N_g = 3, 4$ and 5) and a continuum state describing the incident and scattered electrons (processing of a continuum electron is discussed in [22]). Accordingly, the two-electron wave functions satisfy the following equation

$$(\hat{h}_{\rm D}(\boldsymbol{r}_1) + \hat{h}_{\rm D}(\boldsymbol{r}_2))\Psi_{k_g}^{(0)} = E_{k_g}^{(0)}\Psi_{k_g}^{(0)}. \tag{11}$$

The states with $n > N_g$ are taken into account indirectly through the two-photon exchange corrections in the second order of the QED perturbation theory as the terms in the electron propagator (n_1 and n_2 in b and c graphs figure 1). We demonstrate the effect of the different selections of the set G on the cross section in figure 2.

In this work, we include into matrix V_{11} the following corrections: electron self-energy and vacuum polarization, one-photon and two-photon exchange corrections. For the two-photon exchange correction we take into account only the box diagram (figure 1(b)) within the Breit approximation neglecting the retardation [23].

The matrix V_{11} is a complex symmetric finite matrix. It can be diagonalized numerically:

$$V^{\rm diag} = B^T V_{11} B, \; B^T B = I. \tag{12}$$

The eigenvectors of V_{11} yield the functions Φ_{n_g} corresponding to various states of the atomic system:

$$\Phi_{n_g} = \sum_{k_g \in g} B_{k_g n_g} \Psi_{k_g}^{(0)}, \tag{13}$$

the eigenvalues of V_{11} give the corresponding energies ε_{n_g} and widths Γ_{n_g}:

$$\mathcal{E}_{n_g} = E_{n_g} - \frac{i}{2}\Gamma_{n_g}. \tag{14}$$

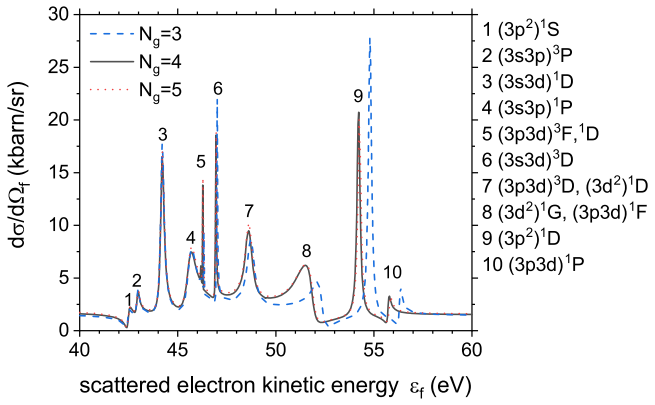

Figure 2. The backward ($\theta = 180°$) differential cross section for the inelastic electron scattering on F^{8+} with the excitation $1s \rightarrow 2s$ for different choices of the set G: blue dashed line corresponds to the set G with $N_g = 3$, black solid line to $N_g = 4$ and red dotted line to $N_g = 5$. The autoionizing states involved in forming the resonances are listed on the right.

The function $\Phi^i_{m_i,\mu_i}(\boldsymbol{r}_1, \boldsymbol{r}_2)$ can be written as

$$\Phi^i_{m_i,\mu_i}(\boldsymbol{r}_1, \boldsymbol{r}_2) = \Psi^i_{m_i,\mu_i}(\boldsymbol{r}_1, \boldsymbol{r}_2) + \sum_{k_g \in G, k_g \in \textbf{bound}} C_{k_g} \Psi^{(0)}_{k_g}(\boldsymbol{r}_1, \boldsymbol{r}_2) + \cdots . \tag{15}$$

where the coefficients C_{k_g} are determined by the matrix B. The term $\Psi^i_{m_i,\mu_i}(\boldsymbol{r}_1, \boldsymbol{r}_2)$ corresponds to the non-resonant channel (1). The orthogonal term $\sum C_{k_g} \Psi^{(0)}_{k_g}(\boldsymbol{r}_1, \boldsymbol{r}_2)$ contains the admixture of the bound states of the ion with two electrons and describes the formation of the intermediate autoionizing states in the resonant channel (2).

Since the Coulomb scattering does not contribute to the inelastic scattering, the amplitude U is determined by the matrix ΔV as [20]

$$U_{if} = \langle \Psi^f_{m_f,\mu_f}(\boldsymbol{r}_1, \boldsymbol{r}_2) | \Delta \hat{V} | \Phi^i_{m_i,\mu_i}(\boldsymbol{r}_1, \boldsymbol{r}_2) \rangle. \tag{16}$$

In 16, only the one-photon exchange corrections were included in the matrix ΔV.

The double differential cross section for the inelastic electron scattering reads [18]

$$\frac{d^2\sigma_{if}}{d\varepsilon_f d\Omega_f}(\varepsilon_f, \theta_f) = 2\pi \frac{1}{4} \sum_{\substack{m_i \mu_i \\ m_f \mu_f}} |U_{if}|^2 \frac{\varepsilon_i}{p_i} \frac{p_f \varepsilon_f}{(2\pi)^3} \times \delta(\varepsilon_f + \varepsilon_{2l} - \varepsilon_i - \varepsilon_{1s}). \tag{17}$$

The results of application of this approach are presented and discussed in the next section.

3. Results and discussion

The method described in the previous section has been developed primarily for medium and high Z systems where the relativistic and QED effects are pronounced. Nevertheless, we can also apply it to the scattering on the light ions where theoretical calculations using the R-matrix method as well as experimental data are available [11–14]. In [14] the comprehensive study of the inelastic scattering in the collision of F^{8+} with molecular hydrogen is presented. Thus, in order to test our approach we start our discussion with the revision of the inelastic electron scattering on hydrogen-like F^{8+} ions studied in [14].

3.1. Inelastic electron scattering on F^{8+}

In the context of the inelastic scattering, the intermediate autoionizing states that contribute to the resonant scattering channel are located within a densely populated energy region. Consequently, careful treatment of the interelectron interaction is necessary. The accuracy of our method is principally determined by the electron states included into the set G. In order to illustrate the relative importance of different electron states we calculated the backward scattering cross section on F^{8+} ion (with the ion excited from $1s$ to $2s$ state) for three choices of the set G. The set G is defined by N_g, which represents the highest principal quantum number among the one-electron states forming the two-electron configurations within the set G. The resulting cross sections for $N_g = 3$, 4 and 5 are presented in figure 2. We find that the differences in the position of the resonances between the choices $N_g = 3$ and $N_g = 4$ are most significant for the higher lying (right side of the graph) resonances. This is expected as the corresponding autoionizing states are getting close in energy to the $3l4l'$ states. Our calculations for $N_g = 5$ show that the inclusion of additional electron states to the set G with $N_g = 4$ does not

Table 1. Energies (E) and widths (Γ) of $3l3l'$ autoionizing states in F^{7+} and corresponding incident electron resonant energies ($\varepsilon_i^{\rm res}$) in eV.

Autoionizing state		F^{7+}		
		E	$\varepsilon_i^{\rm res}$	Γ
$(3p^2)^1S$	$(3p_{3/2}^2)_0$	−233.3	869.9	0.19
	$(3s3p_{1/2})_0$	−232.9	870.3	0.12
$(3s3p)^3P$	$(3s3p_{1/2})_1$	−232.9	870.3	0.12
	$(3s3p_{3/2})_2$	−232.8	870.3	0.12
$(3s3d)^1D$	$(3s3d_{5/2})_2$	−231.6	871.6	0.21
	$(3p_{1/2}^2)_0$	−230.7	872.5	0.20
$(3p^2)^3P$	$(3p_{1/2}3p_{3/2})_1$	−230.6	872.5	0.20
	$(3p_{1/2}3p_{3/2})_2$	−230.6	872.6	0.20
$(3s3p)^1P$	$(3s3p_{3/2})_1$	−230.2	873.0	0.56
	$(3p_{1/2}3d_{3/2})_2$	−229.7	873.5	<0.01
$(3p3d)^3F$	$(3p_{3/2}3d_{3/2})_3$	−229.7	873.5	<0.01
	$(3p_{3/2}3d_{5/2})_4$	−229.6	873.5	<0.01
$(3p3d)^1D$	$(3p_{3/2}3d_{5/2})_2$	−229.5	873.7	0.01
	$(3s3d_{3/2})_1$	−228.9	874.3	0.03
$(3s3d)^3D$	$(3s3d_{3/2})_2$	−228.9	874.3	0.03
	$(3s3d_{5/2})_3$	−228.8	874.3	0.03
	$(3p_{1/2}3d_{3/2})_1$	−227.4	875.7	0.14
$(3p3d)^3D$	$(3p_{3/2}3d_{3/2})_2$	−227.4	875.7	0.14
	$(3p_{3/2}3d_{5/2})_3$	−227.4	875.8	0.14
$(3d^2)^1D$	$(3d_{5/2}^2)_2$	−227.2	876.0	0.46
$(3s^2)^1S$	$(3s^2)_0$	−226.8	876.3	0.76
	$(3d_{3/2}^2)_2$	−226.5	876.6	0.15
$(3d^2)^3F$	$(3d_{3/2}3d_{5/2})_3$	−226.5	876.6	0.15
	$(3d_{5/2}^2)_4$	−226.5	876.7	0.15
	$(3p_{3/2}3d_{3/2})_0$	−226.3	876.9	0.05
$(3p3d)^3P$	$(3p_{3/2}3d_{3/2})_1$	−226.3	876.9	0.05
	$(3p_{1/2}3d_{5/2})_2$	−226.3	876.8	0.05
$(3d^2)^1G$	$(3d_{3/2}3d_{5/2})_4$	−224.5	878.6	1.07
$(3p3d)^1F$	$(3p_{1/2}3d_{5/2})_3$	−224.1	879.0	0.58
	$(3d_{3/2}^2)_0$	−223.5	879.6	<0.01
$(3d^2)^3P$	$(3d_{3/2}3d_{5/2})_1$	−223.5	879.6	<0.01
	$(3d_{3/2}3d_{5/2})_2$	−223.5	879.6	<0.01
$(3p^2)^1D$	$(3p_{3/2}^2)_2$	−221.6	881.6	0.19
$(3p3d)^1P$	$(3p_{3/2}3d_{5/2})_1$	−220.1	883.1	0.15
$(3d^2)^1S$	$(3d_{5/2}^2)_0$	−215.3	887.8	<0.01

significantly change the cross section. Overall, we find that $N_g = 4$ is optimal for the purposes of this work. The fast convergence of the method in respect to N_g is provided by taking into account the interaction with the $n \geqslant 5$ electron states present in the two-photon exchange graph (two right graphs in figure 1).

The energies and widths of the intermediate autoionizing states, as well as the corresponding incident electron resonance energies for F^{8+} are presented in table 1. For F^{8+} we also specify the corresponding LS coupling scheme states. We clearly see that the LS coupling scheme works well in this case. We estimate that the accuracy of our calculations is about 0.1 eV for the resonance energies and 0.005 eV for the widths. At this level of accuracy the widths of the electron states are completely determined by the Auger widths.

The existing experiments have studied the inelastic scattering of electrons in the collision of one-electron ions with a hydrogen molecule, which served as a source of quasi-free electrons [11–14]. In these experiments, no distinction was made between $2s$, $2p_{1/2}$ and $2p_{3/2}$ final ion states. Consequently, the double differential cross sections given in [14] contain contributions from all three channels. Our results presented in figure 3 and discussed below also take into account all possible excitations of the F^{8+} ion.

In order to adapt our method to the description of the ion-atom and ion-molecule collisions, we employ the impulse approximation [24, 25] (see appendix). The relevant double differential cross section reads as

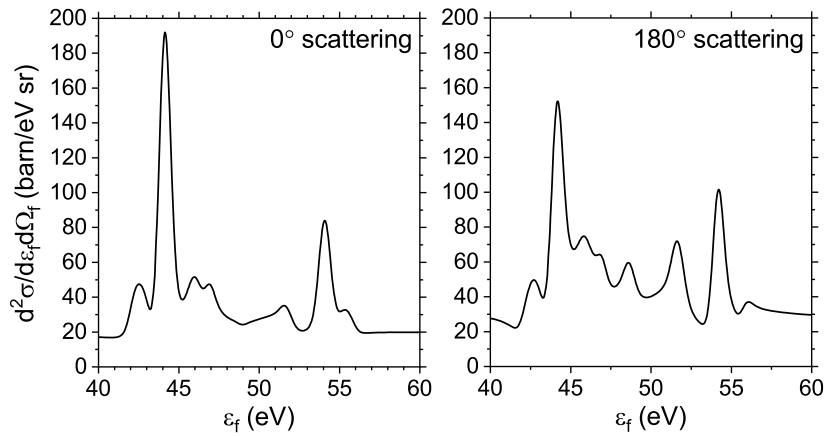

Figure 3. The double differential cross section for the forward (left panel, $\theta = 0°$) and backward (right panel, $\theta = 180°$) inelastic electron scattering on F^{8+} in collision with molecular hydrogen.

Table 2. Energies of the highest-lying $3l3l'$ autoionizing states in F^{7+} in eV. The results for the set G with $N_g = 3$ are presented in the first column. The second column gives the results for $N_g = 4$ except $4f$ electrons are completely excluded from the calculation. The third column gives the results for $N_g = 4$*where*$4f$ electrons are excluded from the set G and are accounted for in the box two-photon exchange correction (figure 1(b)). The values used in this work ($N_g = 4$) are shown in the fourth column and are highlighted in bold. The results for the set G with $N_g = 5$ are presented in the fifth column.

		$N_g = 3$	$N_g = 4$ 4f excluded	$N_g = 4$ 4f partially included	$N_g = 4$	$N_g = 5$
	$(3d_{3/2}^2)_0$	−223.46	−223.42	−223.51	**−223.53**	−223.52
$(3d^2)^3P$	$(3d_{3/2}3d_{5/2})_1$	−223.45	−223.41	−223.50	**−223.52**	−223.51
	$(3d_{3/2}3d_{5/2})_2$	−223.44	−223.40	−223.49	**−223.51**	−223.50
$(3p^2)^1D$	$(3p_{3/2}^2)_2$	−221.43	−220.88	−221.51	**−221.60**	−221.55
$(3p3d)^1P$	$(3p_{3/2}3d_{5/2})_1$	−219.89	−219.22	−219.99	**−220.09**	−220.03
$(3d^2)^1S$	$(3d_{5/2}^2)_0$	−215.04	−214.87	−215.24	**−215.33**	−215.29

$$\frac{d^2\sigma_{H_2}}{d\varepsilon_f d\Omega_f}(\varepsilon_f, \theta_f) = \frac{1}{\gamma\beta} J_{H_2}(p_i) \frac{d\sigma}{d\Omega_f}(\varepsilon_f, \theta_f), \tag{18}$$

where β is the collision velocity, $\gamma = 1/\sqrt{1-\beta^2}$, $J_{H_2}(p_i)$ is the Compton profile of molecular hydrogen obtained experimentally [11].

To compare the cross section 18 with the experimental data, we also need to take into account the experimental resolution. To do this, we convolute the resulting cross sections with the Gaussian function [14]

$$\frac{1}{\sqrt{2\pi}\ \sigma_r} \exp\left(\frac{-(\varepsilon - \varepsilon_f)^2}{2\sigma_r^2}\right), \tag{19}$$

with parameter $\sigma_r = 0.28$ eV corresponding to the experimental resolution.

The resulting forward (upper panel) and backward (lower panel) scattering cross sections for F^{8+} are presented in figure 3. For the spectral region $\varepsilon_f < 50$ eV, our results are in excellent agreement with the experimental data [14]. For the region $\varepsilon_f > 50$ eV, our results are in reasonable agreement. Three right peaks are shifted to the left compared to the data given in [14]. Discrepancies observed in the higher energy region can be attributed to the insufficient accuracy of the calculations. The energies of the rightmost resonances calculated with different choices of the set G are given in table 2. We particularly emphasize the energy shift caused by taking into account the $4f$ electrons which shows that high-l electrons should not be neglected in the calculations. We note that the contribution from the electrons with the principal quantum number $n = 5$ is too small to explain the discrepancy.

Using F^{8+} as an example, we have demonstrated that our method works reasonably well and can be successfully applied even to the light systems. In the next section we consider scattering on heavier ions.

Table 3. Energies (E) and widths (Γ) of $3l3l'$ autoionizing states in Ca^{18+} and corresponding incident electron resonant energies (ε_i^{res}) in eV. Radiative Γ_r and Auger Γ_a widths are given separately in eV in the last two columns.

Autoionizing state		Ca^{18+}				
		E	ε_i^{res}	Γ	Γ_r	Γ_a
$(3p^2)^1S$	$(3p_{3/2}^2)_0$	−1170.7	4299.2	0.78	0.021	0.759
	$(3s3p_{1/2})_0$	−1187.7	4282.2	0.14	0.022	0.117
$(3s3p)^3P$	$(3s3p_{1/2})_1$	−1187.2	4282.7	0.14	0.022	0.122
	$(3s3p_{3/2})_2$	−1185.9	4284.1	0.14	0.022	0.119
$(3s3d)^1D$	$(3s3d_{5/2})_2$	−1171.2	4298.8	0.45	0.015	0.435
	$(3p_{1/2}^2)_0$	−1181.4	4288.6	0.23	0.037	0.197
$(3p^2)^3P$	$(3p_{1/2}3p_{3/2})_1$	−1180.7	4289.2	0.23	0.038	0.196
	$(3p_{1/2}3p_{3/2})_2$	−1182.8	4287.2	0.22	0.028	0.196
$(3s3p)^1P$	$(3s3p_{3/2})_1$	−1179.5	4290.5	0.54	0.024	0.518
	$(3p_{1/2}3d_{3/2})_2$	−1178.6	4291.3	0.03	0.027	0.004
$(3p3d)^3F$	$(3p_{3/2}3d_{3/2})_3$	−1177.3	4292.6	0.03	0.027	0.004
	$(3p_{3/2}3d_{5/2})_4$	−1175.9	4294.0	0.03	0.027	0.002
$(3p3d)^1D$	$(3p_{3/2}3d_{5/2})_2$	−1169.3	4300.6	0.08	0.026	0.056
	$(3s3d_{3/2})_1$	−1176.8	4293.2	0.04	0.008	0.031
$(3s3d)^3D$	$(3s3d_{3/2})_2$	−1176.5	4293.5	0.04	0.008	0.031
	$(3s3d_{5/2})_3$	−1176.1	4293.9	0.04	0.008	0.030
	$(3p_{1/2}3d_{3/2})_1$	−1172.5	4297.4	0.16	0.027	0.133
$(3p3d)^3D$	$(3p_{3/2}3d_{3/2})_2$	−1172.1	4297.8	0.16	0.027	0.128
	$(3p_{3/2}3d_{5/2})_3$	−1171.4	4298.6	0.16	0.027	0.134
$(3d^2)^1D$	$(3d_{5/2}^2)_2$	−1157.0	4312.9	0.21	0.019	0.187
$(3s^2)^1S$	$(3s^2)_0$	−1188.3	4281.7	0.18	0.015	0.165
	$(3d_{3/2}^2)_2$	−1169.3	4300.7	0.17	0.014	0.154
$(3d^2)^3F$	$(3d_{3/2}3d_{5/2})_3$	−1168.9	4301.0	0.16	0.014	0.147
	$(3d_{5/2}^2)_4$	−1168.4	4301.5	0.16	0.014	0.150
	$(3p_{3/2}3d_{3/2})_0$	−1169.3	4300.6	0.08	0.027	0.057
$(3p3d)^3P$	$(3p_{3/2}3d_{3/2})_1$	−1169.4	4300.6	0.08	0.026	0.057
	$(3p_{1/2}3d_{5/2})_2$	−1176.5	4293.4	0.04	0.027	0.009
$(3d^2)^1G$	$(3d_{3/2}3d_{5/2})_4$	−1163.3	4306.7	1.09	0.014	1.072
$(3p3d)^1F$	$(3p_{1/2}3d_{5/2})_3$	−1162.9	4307.0	0.61	0.027	0.579
	$(3d_{3/2}^2)_0$	−1162.5	4307.5	0.02	0.016	0.004
$(3d^2)^3P$	$(3d_{3/2}3d_{5/2})_1$	−1162.3	4307.7	0.02	0.016	0.004
	$(3d_{3/2}3d_{5/2})_2$	−1161.9	4308.0	0.02	0.017	0.005
$(3p^2)^1D$	$(3p_{3/2}^2)_2$	−1179.3	4290.6	0.23	0.037	0.195
$(3p3d)^1P$	$(3p_{3/2}3d_{5/2})_1$	−1153.8	4316.2	0.19	0.024	0.164
$(3d^2)^1S$	$(3d_{5/2}^2)_0$	−1142.2	4327.8	0.03	0.020	0.008

3.2. Inelastic electron scattering on Ca^{19+} and Kr^{35+}

In this section our calculations are performed for the inelastic scattering of free electrons. We consider the energies of incident electrons where the resonance structure of the cross section arises from the contribution of the lowest-lying autoionizing states contributing to the process ($3l3l'$). In this energy range, we can differentiate between three channels of the inelastic electron scattering with the excitation of the ion from the ground state to the $2s$, $2p_{1/2}$ and $2p_{3/2}$ excited states. In contrast to the scattering on the F^{8+} ion, in the case of heavier ions such as Ca^{19+} and Kr^{35+}, the scattered electrons have noticeably distinct final energies depending on the scattering channel. For each scattering channel the scattered electron energy is strictly determined by the incident electron energy (3).

In tables 3 and 4 we present the energies (E) and widths (Γ) of the autoionizing $3l3l'$ states for Ca^{18+} and Kr^{34+} respectively as well as the corresponding resonance energies of the incident electron (ε_i^{res}). For these ions we also give the radiative (Γ_r) and Auger (Γ_a) widths separately. The order of two-electron configurations is carried over from table 1 for F^{7+} ion. The resonance energies of the scattered electron for any scattering channel can be obtained using

Table 4. Energies (E) and widths (Γ) of $3l3l'$ autoionizing states in Kr^{34+} and corresponding incident electron resonant energies (ε_i^{res}) in eV. Radiative Γ_r and Auger Γ_a widths are given separately in eV in the last two columns.

Autoionizing state		Kr^{34+}				
		E	ε_i^{res}	Γ	Γ_r	Γ_a
$(3p^2)^1S$	$(3p_{3/2}^2)_0$	−3869.3	14066.8	1.01	0.332	0.681
	$(3s3p_{1/2})_0$	−3934.7	14001.4	0.33	0.220	0.112
$(3s3p)^3P$	$(3s3p_{1/2})_1$	−3931.2	14005.0	0.37	0.222	0.148
	$(3s3p_{3/2})_2$	−3912.6	14023.5	0.34	0.223	0.117
$(3s3d)^1D$	$(3s3d_{5/2})_2$	−3886.6	14049.5	0.48	0.281	0.201
	$(3p_{1/2}^2)_0$	−3915.6	14020.5	0.55	0.298	0.253
$(3p^2)^3P$	$(3p_{1/2}3p_{3/2})_1$	−3902.8	14033.3	0.61	0.411	0.194
	$(3p_{1/2}3p_{3/2})_2$	−3906.5	14029.7	0.50	0.307	0.197
$(3s3p)^1P$	$(3s3p_{3/2})_1$	−3900.0	14036.2	0.66	0.239	0.418
	$(3p_{1/2}3d_{3/2})_2$	−3900.4	14035.8	0.29	0.286	0.006
$(3p3d)^3F$	$(3p_{3/2}3d_{3/2})_3$	−3866.7	14069.4	0.44	0.281	0.163
	$(3p_{3/2}3d_{5/2})_4$	−3870.0	14066.1	0.29	0.284	0.002
$(3p3d)^1D$	$(3p_{3/2}3d_{5/2})_2$	−3861.8	14074.4	0.35	0.281	0.070
	$(3s3d_{3/2})_1$	−3896.6	14039.5	0.11	0.082	0.033
$(3s3d)^3D$	$(3s3d_{3/2})_2$	−3894.1	14042.0	0.17	0.112	0.055
	$(3s3d_{5/2})_3$	−3889.2	14046.9	0.11	0.080	0.029
	$(3p_{1/2}3d_{3/2})_1$	−3883.0	14053.1	0.40	0.273	0.125
$(3p3d)^3D$	$(3p_{3/2}3d_{3/2})_2$	−3872.4	14063.7	0.36	0.284	0.076
	$(3p_{3/2}3d_{5/2})_3$	−3850.6	14085.5	0.77	0.281	0.494
$(3d^2)^1D$	$(3d_{5/2}^2)_2$	−3836.9	14099.2	0.31	0.173	0.140
$(3s^2)^1S$	$(3s^2)_0$	−3934.8	14001.3	0.33	0.167	0.160
	$(3d_{3/2}^2)_2$	−3861.9	14074.2	0.31	0.158	0.150
$(3d^2)^3F$	$(3d_{3/2}3d_{5/2})_3$	−3857.2	14078.9	0.29	0.147	0.144
	$(3d_{5/2}^2)_4$	−3843.9	14092.2	1.08	0.146	0.933
	$(3p_{3/2}3d_{3/2})_0$	−3865.5	14051.5	0.36	0.283	0.074
$(3p3d)^3P$	$(3p_{3/2}3d_{3/2})_1$	−3865.6	14070.6	0.36	0.279	0.085
	$(3p_{1/2}3d_{5/2})_2$	−3884.6	14070.6	0.33	0.280	0.051
$(3d^2)^1G$	$(3d_{3/2}3d_{5/2})_4$	−3852.6	14083.5	0.41	0.146	0.264
$(3p3d)^1F$	$(3p_{1/2}3d_{5/2})_3$	−3887.8	14048.3	0.33	0.282	0.043
	$(3d_{3/2}^2)_0$	−3849.7	14086.4	0.17	0.154	0.019
$(3d^2)^3P$	$(3d_{3/2}3d_{5/2})_1$	−3846.4	14089.7	0.17	0.155	0.014
	$(3d_{3/2}3d_{5/2})_2$	−3846.3	14089.8	0.24	0.160	0.082
$(3p^2)^1D$	$(3p_{3/2}^2)_2$	−3871.2	14064.9	0.62	0.250	0.366
$(3p3d)^1P$	$(3p_{3/2}3d_{5/2})_1$	−3838.6	14097.5	0.49	0.268	0.217
$(3d^2)^1S$	$(3d_{5/2}^2)_0$	−3810.9	14125.2	0.24	0.197	0.043

Table 5. The energy transfer $\Delta\varepsilon$ in the inelastic electron scattering for $2s$, $2p_{1/2}$ and $2p_{3/2}$ final states of the Ca^{19+} and Kr^{35+} ions in eV.

$\Delta\varepsilon$ (eV)	$\varepsilon_{2s} - \varepsilon_{1s}$	$\varepsilon_{2p_{1/2}} - \varepsilon_{1s}$	$\varepsilon_{2p_{3/2}} - \varepsilon_{1s}$
Ca^{19+}	4100.4	4100.2	4107.6
Kr^{35+}	13430.9	13429.2	13508.8

$$\varepsilon_f^{res} = \varepsilon_i^{res} - (\varepsilon_{2l} - \varepsilon_{1s}), \tag{20}$$

where energy differences $(\varepsilon_{2l} - \varepsilon_{1s})$ can be found in table 5 for each final excited state of the ion. We can see that the increasing importance of spin-orbit interaction for Ca^{18+} and Kr^{34+} makes the jj coupling scheme more suitable for describing autoionizing states. For the heavier element of Kr^{34+}, the spin-orbit interaction is so important that it leads to a significant change in the energy distribution of autoionizing states.

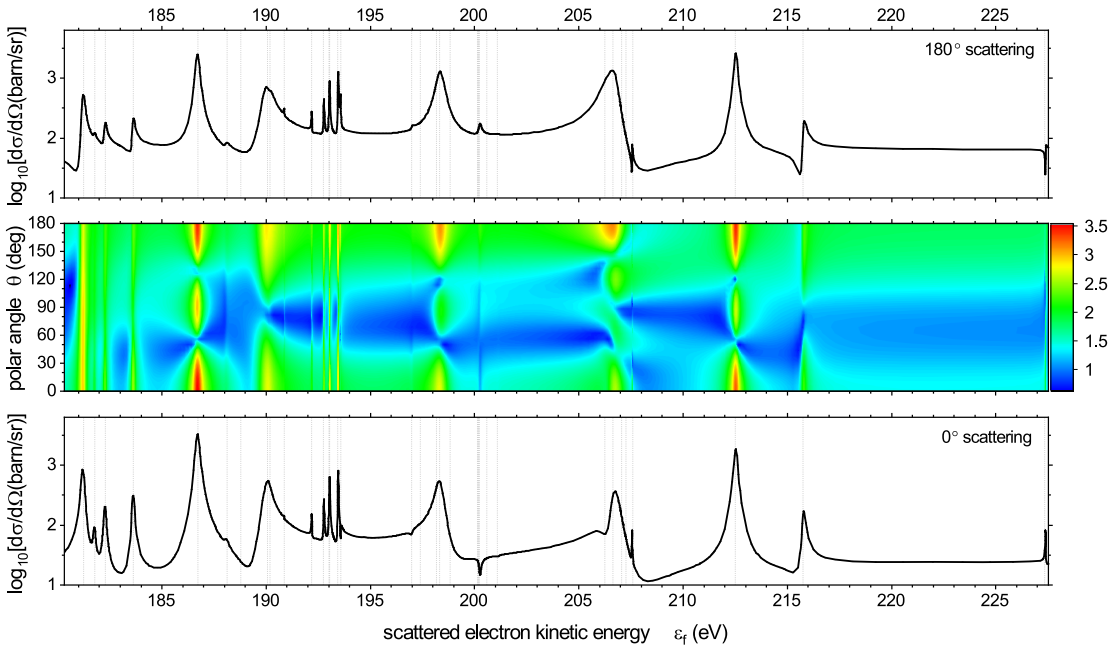

Figure 4. The decimal logarithm of the differential cross section for the inelastic electron scattering on Ca^{19+} as a function of scattering angle θ and scattered electron energy ε_f for the 2*s* final ion state (central panel). Corresponding forward and backward scattering cross sections are presented in the bottom and top panels respectively.

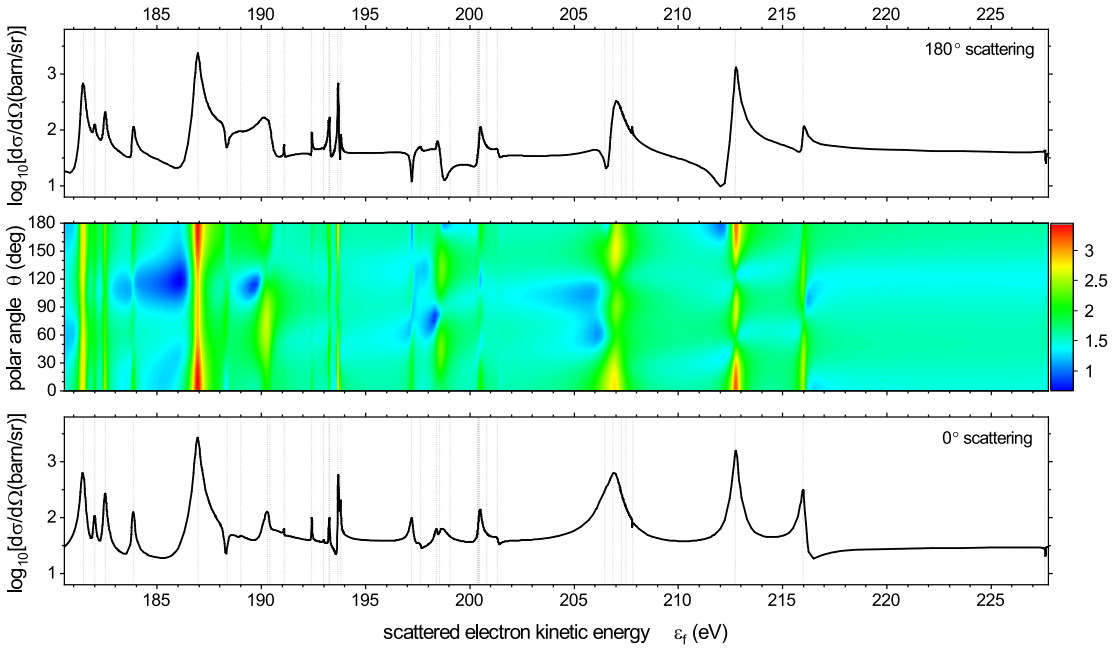

Figure 5. Same as figure 4 but for the $2p_{1/2}$ final state of the ion.

In figures 4–9 we present the differential cross sections for three different channels of scattering on Ca^{19+} and Kr^{35+}. The forward scattering cross sections are shown in the bottom panels, the backward scattering cross sections are demonstrated in the top panels and the cross sections for all scattering angles are presented in the middle panels in a 3D color format. The vertical lines indicate the positions of the resonances corresponding to the energies from tables 3 and 4. The raw numerical data can be found in supplemental materials.

We note that the channels under consideration lead to different final states, particularly in terms of their parity. This results in qualitative differences between the cross sections associated with these channels. In particular, for the final ion state of 2*s* the scattering occurs mainly in the forward and backward directions. The resonance peaks also reach maximum at 0°and 180°. In contrast, for the 2*p* states the angular dependence of the

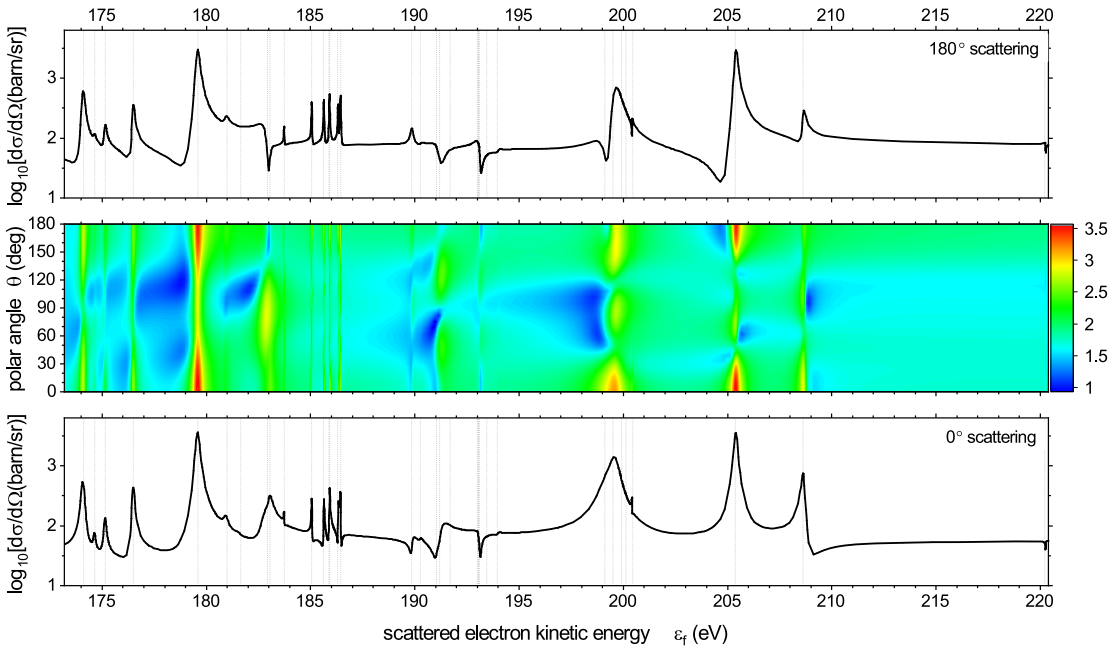

Figure 6. Same as figure 4 but for the $2p_{3/2}$ final state of the ion.

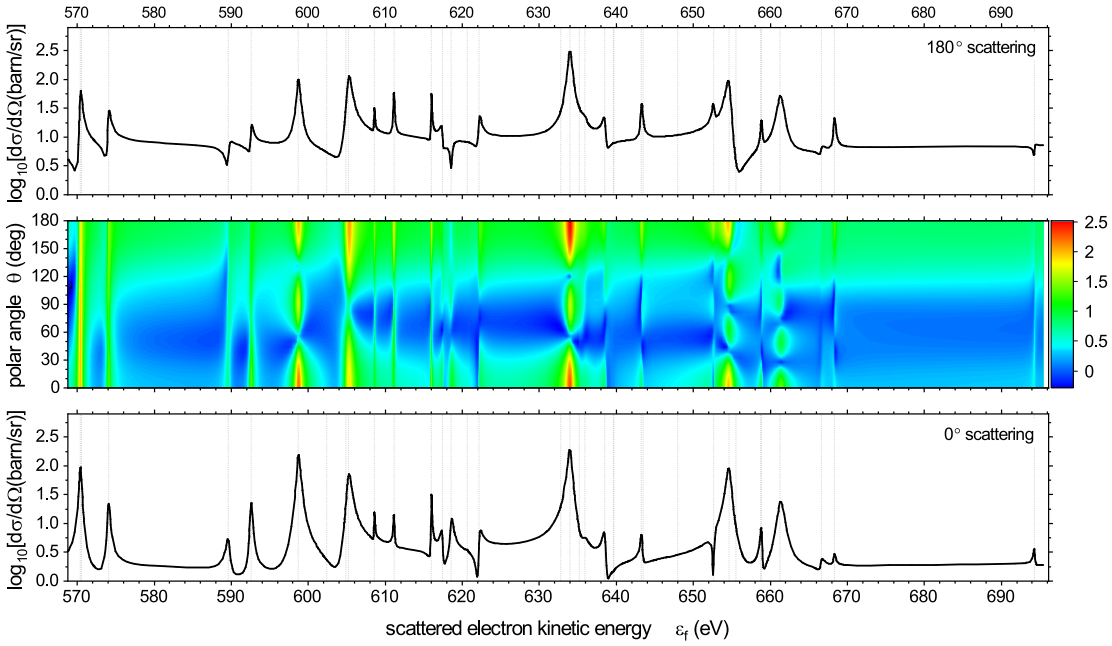

Figure 7. The decimal logarithm of the differential cross section for the inelastic electron scattering on Kr^{35+} as a function of scattering angle θ and scattered electron energy ε_f for the 2*s* final ion state (central panel). Corresponding forward and backward scattering cross sections are presented in the bottom and top panels respectively.

differential cross section changes making scattering into other angles much more significant. For these two channels we can find resonances where electrons tend to scatter to the side.

The comparison of the cross sections for F^{8+}, Ca^{19+} and Kr^{35+} also shows a significant dependence on *Z*. The differences are explained primarily by the different spectra of autoionizing states (see tables 1, 3 and 4). Due to the increased spin-orbit interaction, many previously (in light ions) indistinguishable resonances become separated which leads to the increase in the number of isolated peaks in the cross section.

In collisions involving atoms or molecules we can observe contributions from all possible scattering channels simultaneously as the incident atom or molecule can be regarded as a source of quasi-free electrons with a continuous energy spectrum. In the case of heavier ions, the differences in scattered electron energies for

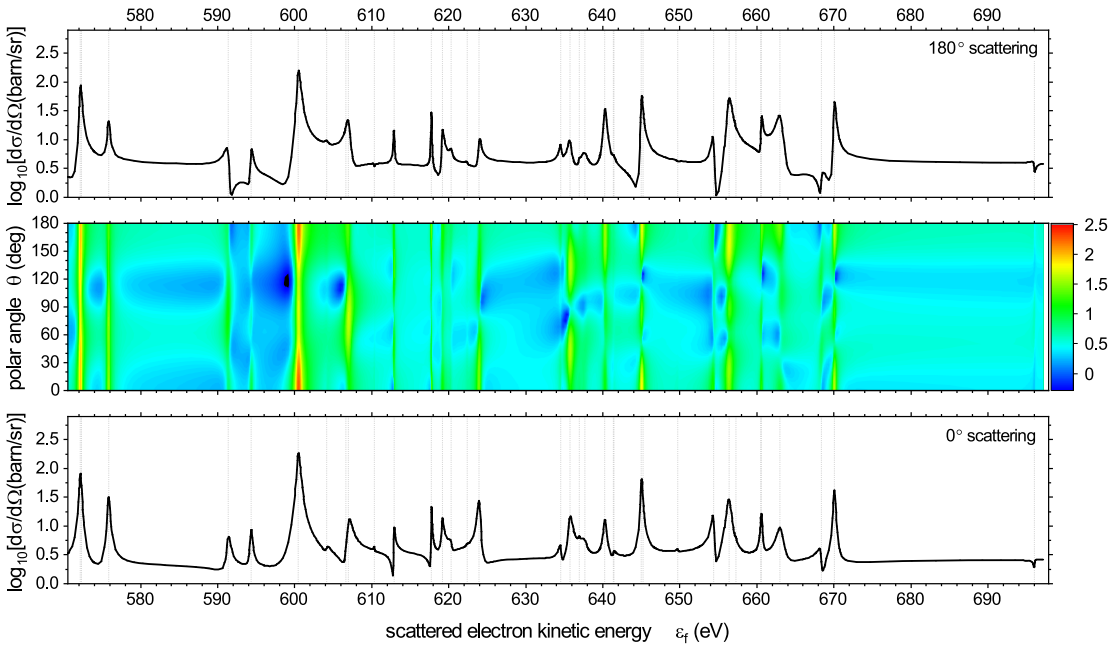

Figure 8. Same as figure 7 but for the $2p_{1/2}$ final state of the ion.

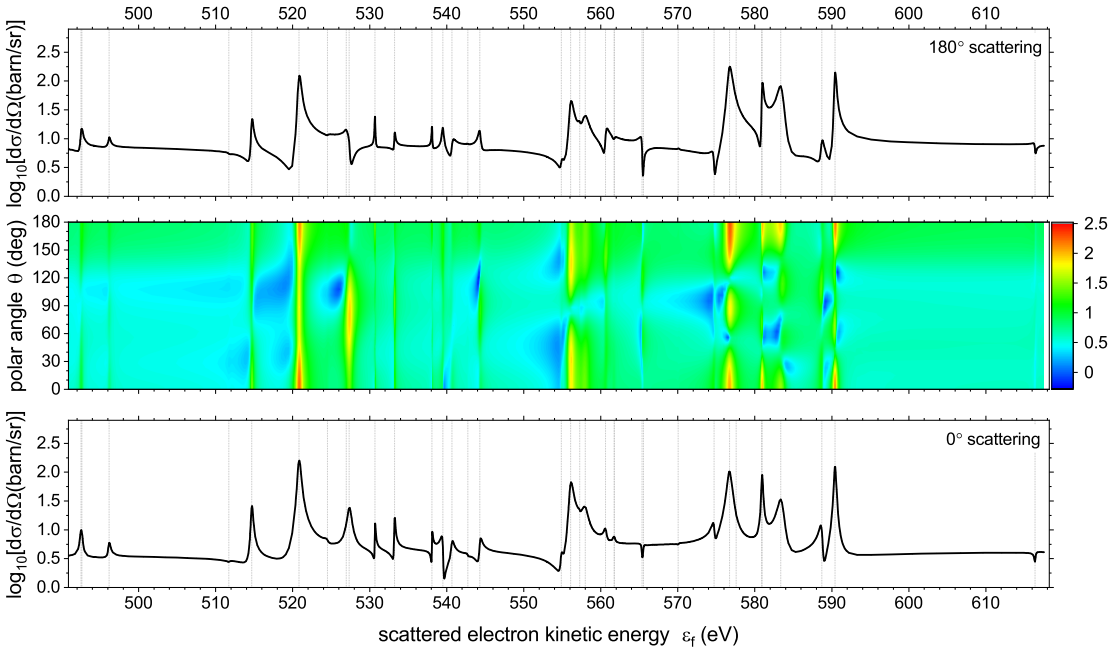

Figure 9. Same as figure 7 but for the $2p_{3/2}$ final state of the ion.

various scattering channels become large compared to the widths of the autoionizing states. Consequently, the cross section for atom-ion or molecule-ion collisions emerges from the partial overlap of resonant structures associated with the three scattering channels. This leads to a significant increase in the complexity of the cross section. Notably, different autoionizing states may contribute to a single peak via different scattering channels. We include complete numerical data for the inelastic electron scattering on Ca^{19+} and Kr^{35+} in the supplemental materials so that the relevant cross sections can be obtained for any experimental setup.

Resonant channel in inelastic scattering substantially alters the overall impact excitation rate, a phenomenon of particular significance in astrophysical investigations of cosmic plasma [4]. We made a rough estimation of the contribution of the resonant channel to the total impact excitation cross section in the energy range of $3l3l'$ resonances. For that purpose we calculated the value of s^{res}, where

Table 6. The estimated contribution from the resonant channel to the total cross section in the energy range where $3l3l'$ autoionizing states are involved (kbarn eV). In the brackets the ratio of the resonant channel to the total cross section is given.

	F^{8+}	Ca^{19+}	Kr^{35+}
$2s$	78.0 (39%)	14.0 (53%)	2.1 (37%)
$2p_{1/2}$	90.9 (35%)	15.9 (49%)	2.4 (36%)
$2p_{3/2}$	177.1 (34%)	12.3 (27%)	0.8 (9%)

$$s^{\mathrm{res}} = \int d\varepsilon_f (\sigma^{\mathrm{total}}(\varepsilon_f) - \sigma^{\mathrm{nonres}}(\varepsilon_f)). \tag{21}$$

The results are presented in table 6 where we also give an approximate share of the resonant channel for the energy range under consideration. Overall, the total cross section of the non-resonant channel varies for different excitations of the ion, being largest for the $2p_{3/2}$ state and smallest for the $2s$ final state. It is notable that the contribution of the resonance structure increases with the nuclear charge Z in a complex manner and also depends on the final state of the ion. In particular, we observe that the relative contribution of the resonant structure for the excitation to $2s$ and $2p_{1/2}$ is larger for Ca^{19+} than for F^{8+} and Kr^{35+}.

4. Conclusions

We developed ab initio QED treatment of the inelastic scattering of quasi-free electrons on hydrogen-like ions with possible formation and subsequent decay of intermediate autoionizing states. The developed method can be applied to a wide range of ions, from relatively light to heavy. Our study focused on the energy range where doubly excited $3l3l'$ states are involved.

We revised the theoretical description of the inelastic scattering on F^{8+} ions presented in [14]. For this purpose, we calculated the double differential forward and backward inelastic scattering cross section in the collision of molecular hydrogen with F^{8+} and compared our results with previous theoretical calculations as well as the experimental data. We also explored the importance of accounting for the interelectron interaction of $n\leqslant 4$ and $n\leqslant 5$ electrons nonperturbatively.

The developed method was subsequently applied to the scattering on heavier ions, yielding the differential cross sections for the inelastic scattering on Ca^{19+} and Kr^{35+} for three scattering channels leading to the excitation of ions into $2s$, $2p_{1/2}$ and $2p_{3/2}$ states. The results for Ca^{19+} and Kr^{35+} ions demonstrate that variations in final states result in substantial qualitative differences in the cross sections across different channels, in particular for the final states with different parities. Furthermore, we investigated the resonant structure and demonstrated that the inelastic scattering cross sections exhibit non-trivial dependence on the atomic number Z in regards to the energy distribution of the autoionizing states and the relative contribution of the resonant channel.

Additionally, the energies and widths of the $3l3l'$ doubly excited states in F^{7+}, Ca^{18+} and Kr^{34+} were calculated. The results obtained emphasise the increasing importance of the spin-orbit interaction with increasing Z.

Acknowledgments

D.M.V. expresses gratitude for the hospitality of the Institute of Modern Physics of CAS during her visit. The work of O.Y.A., K.N.L., D.M.V. in part of the calculation of the cross section was supported solely by the Russian Science Foundation under Grant No. 22-12-00043. O.Y.A. and K.N.L. were supported by the Chinese Academy of Sciences (CAS) Presidents International Fellowship Initiative (PIFI) under Grant Nos. 2018VMB0016 and 2022VMC0002, respectively.

Data availability statement

The data cannot be made publicly available upon publication because they are not available in a format that is sufficiently accessible or reusable by other researchers. The data that support the findings of this study are available upon reasonable request from the authors.

Appendix

The impulse approximation is a useful tool for dealing with processes occurring in asymmetric ion-atom and ion-molecule collisions when the process in question can be considered with a high degree of accuracy as involving only one electron from the atom or molecule [26]. In this case, the atomic or molecular target can be adequately described by a quasi-free electron beam with the initial momentum distribution determined by the internal structure of the system neglecting further interactions with atomic nuclei or other bound electrons. Starting from the one-electron approximation for the atomic or molecular target, we introduce the relation between the wave functions of the bound electron with the ionization energy ε_b in the target rest frame (O') in coordinate $\Psi'(\boldsymbol{r}')$ and momentum $\Phi_i(\boldsymbol{\lambda})$ representations:

$$\Psi'(\boldsymbol{r}') = \frac{1}{(2\pi)^{3/2}} \int d^3\boldsymbol{\lambda}\ \Phi_i(\boldsymbol{\lambda}) \exp(i\boldsymbol{\lambda}\boldsymbol{r}'). \tag{A1}$$

The physical meaning of $\boldsymbol{\lambda}$ is the momentum of the target electron in the target rest frame.

Our first approximation is to neglect the real trajectory of the target. We assume that in the rest frame of the ion (O) the target is moving with the velocity β along the z-axis. In order to transition to the rest frame of the ion, we use the Lorentz transformations

$$t' = \gamma(t - \beta z) \tag{A2}$$

$$z' = \gamma(-\beta t + z),\ \ x' = x,\ \ y' = y \tag{A3}$$

to obtain the vector $\boldsymbol{r}_e$ pointing from the center of mass of the target to the bound electron in the rest frame of the ion and represent the vector $\boldsymbol{r}$ of the bound electron in the rest frame of the ion as

$$\boldsymbol{r} = \boldsymbol{r}_a + \boldsymbol{r}_e, \tag{A4}$$

where $\boldsymbol{r}_a$ is the vector of the target center of mass in the rest frame of the ion. We also neglect transverse electron momentum projections λ_x and λ_y (this is the second approximation) so below we assume that the momentum of the incident electron is directed along z so that $\boldsymbol{p} = p_z\boldsymbol{e}_z$. Thus, the resulting expression for the incident electron wave function $\Psi_i(\boldsymbol{r})$ can be written as follows:

$$\Psi_i(\boldsymbol{r}) = \frac{1}{(2\pi)^{3/2}} \int dp_z e^{i\boldsymbol{p}\boldsymbol{r}} \times \frac{1}{\sqrt{\gamma}} \int d\lambda_x d\lambda_y \Phi_i(\boldsymbol{\lambda}) e^{-i\lambda_x x_a} e^{-i\lambda_y y_a}, \tag{A5}$$

$$p = p_z = \gamma(\lambda_z + \beta\varepsilon_b). \tag{A6}$$

We introduce function $j(p, x, y)$ depending on the electron momentum and the impact parameter:

$$j(p,\, x_a,\, y_a) = \frac{1}{\sqrt{\gamma}} \int d\lambda_x d\lambda_y \Phi_i(\boldsymbol{\lambda}) e^{-i(\lambda_x x_a + \lambda_y y_a)}. \tag{A7}$$

Then for the $\Psi_i(\boldsymbol{r})$ we have the following expansion:

$$\Psi_i(\boldsymbol{r}) = \int dp\ \Psi_{\boldsymbol{p}}^{(Z=0)}(\boldsymbol{r}) j(p,\, x_a,\, y_a), \tag{A8}$$

where $\Psi_{\boldsymbol{p}}^{(Z=0)}(\boldsymbol{r}) = \frac{1}{(2\pi)^{3/2}} e^{i\boldsymbol{p}\boldsymbol{r}}$ is the wave function of free electron with certain momentum $\boldsymbol{p}$ and energy $\varepsilon = \gamma(\varepsilon_b + \beta\lambda_z)$ in the ion rest frame. In the impulse approximation we replace $\Psi_{\boldsymbol{p}}^{(Z=0)}(\boldsymbol{r})$ with $\Psi_{\boldsymbol{p}}(\boldsymbol{r})$ - wave function of the electron in the field of the ion with asymptotic momentum $\boldsymbol{p}$ (6):

$$\Psi_i(\boldsymbol{r}) = \int dp\ \Psi_{\boldsymbol{p}}(\boldsymbol{r}) j(p,\, x_a,\, y_a). \tag{A9}$$

The electron scattering is one of the processes where the energy transfer to the target can be neglected. Therefore, from now on we assume that the initial and final energies of the electron satisfy some variation of the energy conservation law:

$$\varepsilon_f = \varepsilon_i + \Delta\varepsilon, \tag{A10}$$

and the corresponding amplitude can be written as:

$$U(\boldsymbol{p}_i, \boldsymbol{p}_f) = U(\boldsymbol{p}_f)\delta(\varepsilon_f - \varepsilon_i - \Delta\varepsilon). \tag{A11}$$

Since we neglect the transverse components of the incident electron momentum, the energy conservation law implies that for a given energy of the scattered electron the incident electron momentum is fixed:

$$p_z = p_i = \sqrt{\varepsilon_i^2 - 1},\ \ p_x = 0,\ \ p_y = 0. \tag{A12}$$

The amplitude of the process under consideration in the ion-atom collision then can be written as:

$$U_{if}(x, y) = \int dp\ U(\boldsymbol{p}, \boldsymbol{p}_f) j(p, x_a, y_a) = \frac{\varepsilon_i}{p_i} U(\boldsymbol{p}_i, \boldsymbol{p}_f) j(p_i, x_a, y_a). \tag{A13}$$

We are interested in the square of the amplitude absolute value averaged over all impact parameters (x_a and y_a):

$$\begin{aligned} \frac{1}{2\pi} \int dxdy\ |U_{if}(x, y)|^2 &= \frac{\varepsilon_i^2}{2\pi\gamma p_i^2} |U(\boldsymbol{p}_i, \boldsymbol{p}_f)|^2 \\ &\times \int d\lambda_x d\lambda_y \int d\lambda'_x d\lambda'_y \Phi_i(\boldsymbol{\lambda}) \Phi_i^*(\boldsymbol{\lambda}') \\ &\times \int dx_a dy_a e^{i(\lambda'_x - \lambda_x) x_a} e^{i(\lambda'_y - \lambda_y) y_a} \end{aligned} \tag{A14}$$

$$= \frac{\varepsilon_i^2}{\gamma p_i^2} |U(\boldsymbol{p}_i, \boldsymbol{p}_f)|^2 J(p_i), \tag{A15}$$

where we introduce the Compton profile $J(p)$ of the bound electron:

$$J(p) = \int d\lambda_x d\lambda_y |\Phi_i(\boldsymbol{\lambda})|^2. \tag{A16}$$

The Compton profile $J(p)$ gives the distribution of the z-projection of the incident electron momentum. In equation (A15) the Compton profile corresponds to one of the one-electron orbitals of the target. For atoms or molecules with multiple electrons, the one-electron Compton profile $J_t(p)$ must describe the momentum distribution of all electrons in the target. The cross section then reads:

$$\frac{d^2\sigma^{\text{target}}}{d\varepsilon_f d\Omega_f}(\varepsilon_f, \theta_f) = \frac{1}{\gamma\beta} J_t(p_i) \frac{d\sigma^{\text{free}}}{d\Omega_f}(\varepsilon_f, \theta_f) \tag{A17}$$

In this work, we use the approximation for the Compton profile of the hydrogen molecule obtained from experimental data [11].

ORCID iDs

D M Vasileva https://orcid.org/0000-0002-5385-1592
K N Lyashchenko https://orcid.org/0000-0001-7155-1393
O Yu Andreev https://orcid.org/0000-0003-1464-0060
D Yu https://orcid.org/0000-0003-1311-6355

References

[1] Aumayr F, Facsko S, El-Said A S, Trautmann C and Schleberger M 2011 *Journal of Physics: Condensed Matter* **23** 393001
[2] Gault B, Moody M P, Cairney J M and Ringer S P 2012 *Atom Probe Microscopy* (Springer)
[3] Versolato O O 2019 *Plasma Sources Science and Technology* **28** 083001
[4] (Hitomi Collaboration) 2018 *Publications of the Astronomical Society of Japan* **70** 12
[5] Aggarwal K M and Kingston A E 1992 *Physica Scripta* **46** 193
[6] Kisielius R, Berrington K A and Norrington P H 1996 *Astron. Astrophys. Suppl. Ser.* **118** 157–62
[7] Ballance C P, Badnell N R and Berrington K A 2002 *Journal of Physics B: Atomic, Molecular and Optical Physics* **35** 1095
[8] Malespin C, Ballance C P, Pindzola M S, Witthoeft M C, Kallman T R and Loch S D 2011 *A&A* **526** A115
[9] Li S, Yan J, Li C Y, Si R, Guo X L, Huang M, Chen C Y and Zou Y M 2015 *A&A* **583** A82
[10] Mao J, Zanna G D, Gu L, Zhang C Y and Badnell N R 2022 *The Astrophysical Journal Supplement Series* **263** 35
[11] Toth G, Grabbe S, Richard P and Bhalla C P 1996 *Phys. Rev.* A **54** R4613–6
[12] Grabbe S, Toth G, Bhalla C and Richard P 1997 *Nuclear Instruments and Methods in Physics Research Section B: Beam Interactions with Materials and Atoms* **124** 347–9
[13] Závodszky P, Richard P and Bhalla C 1999 *Nuclear Instruments and Methods in Physics Research Section B: Beam Interactions with Materials and Atoms* **154** 153–65
[14] Závodszky P A, Tóth G, Grabbe S R, Zouros T J M, Richard P, Bhalla C P and Tanis J A 1999 *Journal of Physics B: Atomic, Molecular and Optical Physics* **32** 4425
[15] Richard P, Bhalla C, Hagmann S and Zavodszky P 1999 *Physica Scripta* **1999** 87
[16] (GSI Helmholtzzentrum fr Schwerionenforschung D and FAIR GmbH D) 2023 *GSI-FAIR Scientific Report 2022 (GSI Report vol 2023-1)* (GSI Helmholtzzentrum fr Schwerionenforschung GmbH)

[17] Zhou X, Yang J and (the HIAF project team) 2022 *AAPPS Bull* **32** 35
[18] Akhiezer A I and Berestetskii V B 1965 *Quantum Electrodynamics* (Wiley)
[19] Andreev O Y, Labzowsky L N, Plunien G and Solovyev D A 2008 *Physics Reports* **455** 135–246
[20] Lyashchenko K N, Vasileva D M, Andreev O Y and Voitkiv A B 2020 *Phys. Rev. Research* **2** 013087
[21] Furry W H 1951 *Phys. Rev.* **81** 115
[22] Andreev O Y, Labzowsky L N and Prigorovsky A V 2009 *Phys. Rev.* A **80** 042514
[23] Lindgren I, Persson H, Salomonson S and Labzowsky L 1995 *Phys. Rev.* A **51** 1167–95
[24] Montenegro E C and Zouros T J M 1994 *Phys. Rev.* A **50** 3186–91
[25] Benis E P, Zouros T J M, Gorczyca T W, González A D and Richard P 2004 *Phys. Rev.* A **69** 052718
[26] Voitkiv A and Ullrich J 2008 *Relativistic Collisions of Structured Atomic Particles* (Springer)